Research Article Vol. 28, No. 2 / 20 January 2020 / Optics Express 1357

Optics EXPRESS

Nanoparticle trapping and routing on plasmonic nanorails in a microfluidic channel

SHENGQI YIN, FEI HE, NICOLAS GREEN, AND XU FANG*

School of Electronics and Computer Science, University of Southampton, SO17 1BJ, UK
**x.fang@soton.ac.uk*

Abstract: Plasmonic nanostructures hold great promise for enabling advanced optical manipulation of nanoparticles in microfluidic channels, resulting from the generation of strong and controllable light focal points at the nanoscale. A primary remaining challenge in the current integration of plasmonics and microfluidics is to transport trapped nanoparticles along designated routes. Here we demonstrate through numerical simulation a plasmonic nanoparticle router that can trap and route a nanoparticle in a microfluidic channel with a continuous fluidic flow. The nanoparticle router contains a series of gold nanostrips on top of a continuous gold film. The nanostrips support both localised and propagating surface plasmons under light illumination, which underpin the trapping and routing functionalities. The nanoparticle guiding at a Y-branch junction is enabled by a small change of 50 nm in the wavelength of incident light.

1. Introduction

Introducing nanophotonic components into microfluidic channels to achieve novel nanoparticle manipulation is an active, current research area [1]. As compared to traditional optical tweezers, which rely on the use of microscope objectives with a high numerical aperture, nanophotonics-based approaches have many advantages for optofluidic applications in aspects including device miniaturisation and detection throughput [2]. These advantages originate from the near-field focusing enabled by the nanophotonic components, which in most cases is achieved without focusing the incident light beam. Lensless near-field focusing circumvents the diffraction limit that is imposed on far-field focusing, creating extreme intensity focal points at the nanoscale. This property is beneficial for many applications, in particular biological applications that require efficient nanoparticle trapping under relatively low laser intensity [3,4].

Near-field particle manipulation has been demonstrated in a range of different nanophotonic devices that support evanescent optical fields, which include waveguides [5–7], microring resonators [8], whispering gallery mode resonators [9], photonic crystals [10–12], all-dielectric nanoantennas [13] and plasmonic resonators [14–16]. One area which has recently attracted particular attention from the research community, is the use of surface plasmons, a hybridised oscillation of free electrons and light at the surface of a metal. Surface plasmons have two key characteristics, strong light focusing capability (down to volumes below 1 nm^3 has been demonstrated with low loss [17]) and fine tunability, by controlling various properties of incident light (e.g. the wavelength, the polarisation, the orbital angular momentum [18], and the relative phase and polarisation of multiple coherent beams [19,20]). While surface plasmons have been widely investigated for applications outside the context of optofluidics, exploiting them for microfluidics is relatively recent, which has led to the emergence of a new research field, so-called plasmofluidics [14–16].

Plasmonic trapping, i.e. trapping of nanoparticles in plasmonic near field excited by incident light, has been demonstrated using metallic nanostructures [21–27]. A key remaining challenge in plasmonics-microfluidics integration is to transport a trapped nanoparticle in a flow through microfluidic channel. Many different approaches have been explored to achieve this higher level of plasmonic nanoparticle manipulation, which rely on changing the location of plasmonic

#384748 https://doi.org/10.1364/OE.384748
Journal © 2020 Received 2 Dec 2019; revised 29 Dec 2019; accepted 29 Dec 2019; published 8 Jan 2020

focal spots by adjusting the properties (e.g. the wavelength, polarisation and wavefront) of the incident light [28–35]. As the nanoparticle traces the trajectory of the focal spots, it moves in the microchannel while remaining trapped. These plasmonic optical tweezers use only the plasmonic force for the nanoparticle transport, which often results in limited efficiency in nanoparticle delivery. Combining the plasmonic force with other forces can increase the efficiency, but requires precise control over multiple fields (e.g. electromagnetic, electric and thermal fields) at the nanoscale simultaneously [36,37].

This paper presents the concept that in a continuous-flow microchannel, nanoparticle transport can be achieved by using the plasmonic force to guide and route nanoparticles along predefined paths. This approach retains the simplicity of all-optical nanoparticle trapping and utilises the liquid flow to improve the efficiency of nanoparticle delivery. Numerical simulation is used to demonstrate a structure through which a nanoparticle can travel along either one of two predefined paths, with the path selection enabled by a small shift of 50 nm in the incident wavelength. As most lab-on-a-chip devices require continuous-flow microchannels, this plasmon-guided nanoparticle transport mechanism has the potential for numerous applications including biosensing, nanoparticle drug delivery, single-molecule biophysics and nano-assembly.

2. Structure and functionality of the plasmonic nanoparticle router

Figure 1 illustrates the structure of the plasmonic nanorail router. The router consists of several sets of gold nanorails and gratings on a gold thin film at the bottom of a microfluidic channel. Each set of rails is a pair of identical strips separated by a constant gap, and each set of gratings has seven identical, evenly spaced strips. Except for the Y-branch junction where the Entrance Route splits into Route 1 and Route 2, all the strips are along the y direction. At the junction, both gratings follow the associated route in their planar curvature, keeping the grating-rail distance as a constant. This distance is the only difference between the dimensions of the two routes, and it is a critical parameter in producing controllable nanoparticle routing.

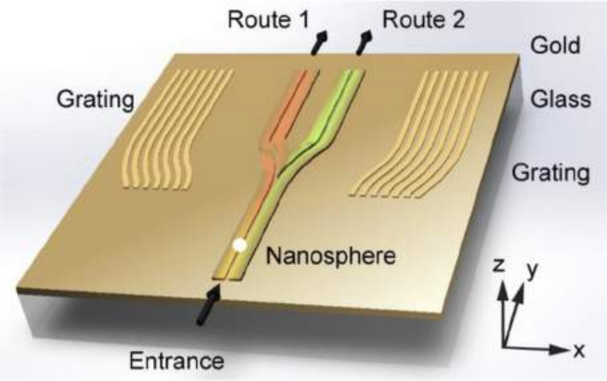

Fig. 1. Schematic diagram of the plasmonic nanoparticle router. The router is a nanostructured, continuous Au thin film on top of a glass substrate. The entrance to the router consists of a pair of nanorails/nanostrips, which then diverges into two routes (Routes 1 and 2) via a Y-branch junction. Two gratings, each consisting of seven strips, are aligned with the outer edges of Routes 1 and 2. The whole router is at the bottom of a microchannel, and it is illuminated by a collimated beam of light at normal incidence from above. A nanoparticle (the white sphere), which moves relatively slowly along the y direction with the fluid above the router, will be confined to the vicinity of the nanorails due to the plasmonic near field (highlighted in red and green). The intention is that the particle will follow either Route 1 or Route 2, depending on the incident wavelength.

A functional router for continuous-flow microchannels is required to confine a nanoparticle in a predefined route with the nanoparticle driven forward by the surrounding liquid, while also allowing for a selection from multiple routes. The wavelength-controlled router presented in this paper satisfies both requirements, with the plasmonic focusing providing the routes and a slight wavelength change selecting the route. The design is developed specifically to function at two wavelengths in the near-infrared (1224 nm and 1274 nm), chosen based on the availability of laser sources for future experiments [38], as well as a low absorption by the water used as the carrier fluid.

In order to determine the performance of the plasmonic router for nanoparticle trapping and routing, the electromagnetic properties were numerically calculated using a 3D finite-element solver (COMSOL Multiphysics). The permittivity of gold was taken from Ref. [39], which was $-69.9+5.6i$ and $-76.4+6.2i$ at 1224 nm and 1274 nm, respectively. The liquid in the microfluidic channel was pure water with a refractive index of 1.33. The material of the substrate was set as glass, albeit as the light did not penetrate through the gold film its permittivity had no influence on the numerical simulation. The flat gold thin film above the glass substrate had a thickness of 300 nm. Due to the high thermal conductivity of gold (317 $\mathrm{W{\cdot}K^{-1}{\cdot}m^{-1}}$) as compared to glass ($\sim$ 1 $\mathrm{W{\cdot}K^{-1}{\cdot}m^{-1}}$), this relatively thick gold film enabled quick heat dissipation, suppressing thermal influences on the trapping even at plasmonic resonances [40].

The performance of the plasmonic router was benchmarked using a polycarbonate nanosphere (refractive index = 1.58, diameter = 220 nm). The incident light was set as a plane wave illuminating the router from above at normal incidence, with both linear and circular polarisation investigated. Light reflection at the air-water interface was not considered. The near-field electric field distribution was simulated without the nanoparticle. The optical force was found by integrating the Maxwell stress tensor at the surface of the nanoparticle. The trapping potential at each location was the line integral of the optical force along a straight path, starting from a location with no discernible near-field enhancement. In the simulation, the start points corresponded to the centre of the nanosphere 300 nm above the top of the nanorails. The cross-sections of the Entrance Route, Route 1 and Route 2 were simulated in 2D, perpendicular to the direction of flow (y direction) for a better analysis of the system far from the Y-branch junction. The full 3D Y-junction was then simulated for the detailed analysis of the performance of the router.

3. Nanoparticle trapping at the Entrance Route

Figure 2 shows the nanoparticle trapping performance along the Entrance Route. Figure 2(a) describes the cross-sectional structure of the nanorails: a pair of gold nanostrips (440 nm in width, 110 nm in height, separated by a gap of 150 nm) on top of a 300 nm thick gold thin film. Figures 2(b) and 2(c) show the numerically simulated electric field distribution with the incident wavelength at 1224 nm and 1274 nm, respectively. Here, only x-polarised incident light is considered, as y-polarised light does not induce any noticeable near field enhancement at these wavelengths. Both figures show strong field enhancement between the two nanorails that resemble a pair of tweezers. A nanoparticle suspended in aqueous solution above the nanorails will be trapped between the two nanorails. The two figures are also almost identical, suggesting that the trapping performance at these two wavelengths is similar.

Figures 2(d) and 2(e) show extracts of the optical potential energy and the optical force along the x axis (F_x) along the dashed line from one side of the rails, across the trapping region, to the other side. The position $x=0$ (the centre of the gap between the two nanorails) is the stable position for both wavelengths: the potential is lowest and $F_x=0$ at this point. The depth of the trap, taken as the difference between the lowest point at $x=0$ and the highest point at $x=\pm 325$ nm, is 6.51 $\mathrm{k_B{\cdot}T/(mW{\cdot}\mu m^{-2})}$ and 7.66 $\mathrm{k_B{\cdot}T/(mW{\cdot}\mu m^{-2})}$ for 1224 nm and 1274 nm, respectively. Here k_B is the Boltzmann constant, and T is 297.15 K. Figure 2(d) also shows two shallow trapping wells at $x \approx \pm 600$ nm, which correspond to the field enhancement at the outer edges of

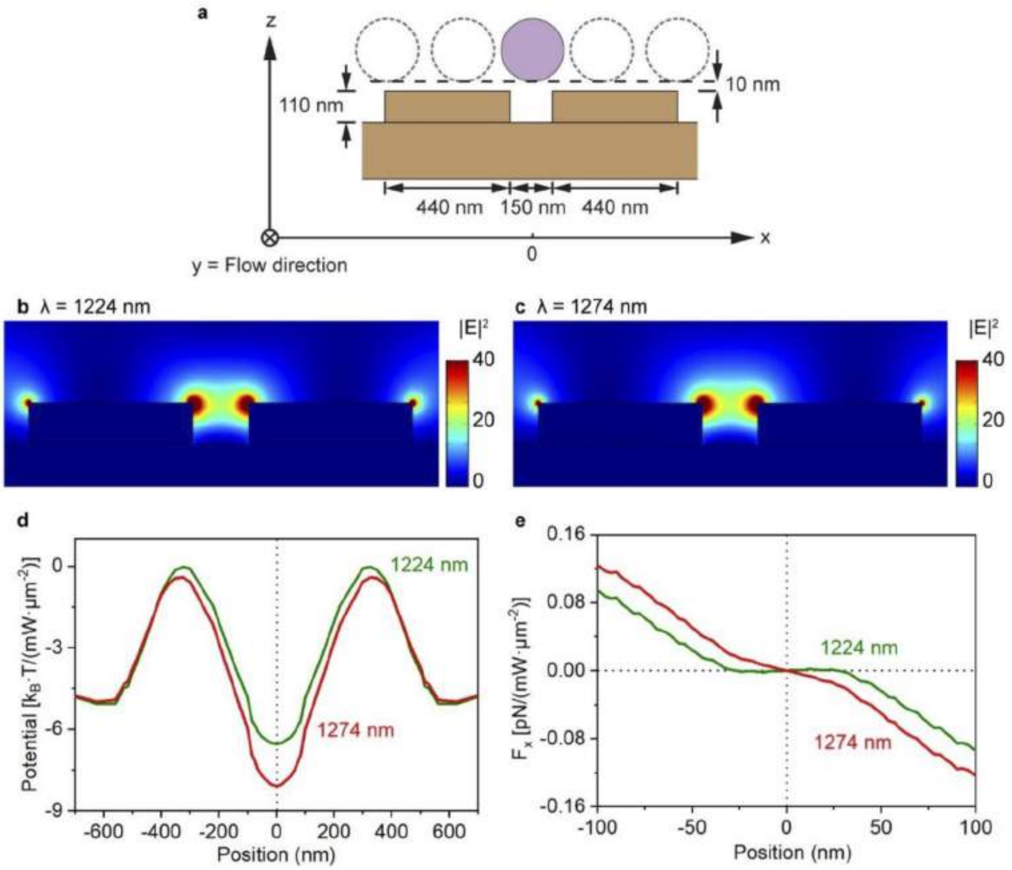

Fig. 2. Nanoparticle trapping characteristics of the entrance nanorails. (a) Schematic of the cross section of the Entrance Route, consisting of two gold nanorails on a thick gold film and a nanoparticle suspended in water above the nanorails. The incident light is polarised along the x axis, i.e. orthogonal to the nanorails. The bottom of the nanoparticle is 10 nm above the top of the nanorails as indicated by the dashed circles. The solid, purple circle indicates the stable position. (b) Enhancement factor of the electric field density at 1224 nm as normalised against the incident field, with the upper limit of colour scale set at 40 for visualisation. (c) Corresponding distribution at 1274 nm using the same colour scale. (d) Dependence of trapping potential on the x position of the nanoparticle, under the illumination of light at 1224 nm (green line) or 1274 nm (red line). (e) Corresponding optical force along the x axis, F_x, at these two wavelengths.

the rails in Figs. 2(b) and 2(c). The curves of the potential and the force (Figs. 2(d) and 2(e), as well as in several other following figures) demonstrate small fluctuations, which are due to numerical error.

4. Nanoparticle trapping at Route 1 and Route 2

The degree of similarity for the two wavelengths of interest shown in Fig. 2 changes once a grating is placed by the side of the nanorails, as demonstrated by simulation in Fig. 3. The grating consists of seven gold nanostrips, for which the periodicity, the width and the height of the nanostrips are fixed values of 400 nm, 200 nm and 70 nm, respectively, while the rail-grating distance d is a free parameter. Plasmonic trapping strongly depends on near-field enhancement, and the effect can be analysed by examining the electric field at the centre point between the two rails, as shown in Fig. 3(b). For both wavelengths the enhancement factor for the electric field oscillates with the distance *d*. This oscillation is the result of the interference between the localised surface plasmons supported by the rails (Fig. 2) and the propagating surface plasmon polaritons generated by the grating. The grating functions as an antenna that converts the incident light into surface plasmons, which then propagate over the distance *d* to the centre test point. Changing the distance *d* produces a variation between constructive interference and destructive interference at the test point. The interference between localised and propagating surface plasmons has been studied previously in the context of extraordinary optical transmission, mainly in a slit-groove configuration [41]. This work presents a similar configuration of rail-grating designed to exploit the near-field enhancement. Similar to prior work, the height of the gratings has been adjusted to optimise device performance.

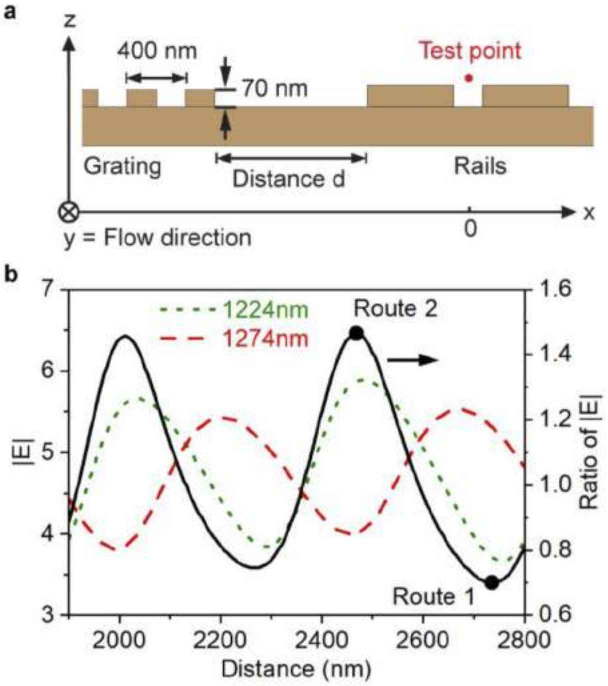

Fig. 3. Route1 and Route 2 adopt a side grating to affect the nanoparticle trapping. (a) Schematic diagram of the pair of nanorails and the side grating. The grating consists of seven nanostrips that are slightly smaller in height than the rails. (b) At both wavelengths of 1224 nm (green dotted line) and 1274 nm (red dashed line), the electric field at the test point (in the middle between the two rails and 10 nm above their tops) oscillates with *d*, the distance between the rail and the grating. The field is normalised against the incident light, which is *x*-polarised. The ratio of the normalised electric field at these two wavelengths is drawn as the black line, on which the values of the distance *d* in Routes 1 and 2 are specified using the two black dots.

Key to the operation of the device is the contrast between the two wavelengths of interest. Although both wavelengths show oscillatory dependence on the distance *d*, the oscillation is different in both phase and amplitude, resulting from multiple sources including the dispersion of both types of surface plasmons. Figure 3 also shows the ratio of the field enhancement to highlight the contrast between these two wavelengths. Over the range of distance *d* investigated here, the ratio varies between 1.47 and 0.70, which correspond to stronger enhancement at 1224 nm and 1274 nm, respectively. These two extreme ratio values are used to determine the geometry of the two routes as discussed below.

Route 1 is designed as the route for the nanoparticle at wavelength $\lambda = 1274$ nm. The rail-groove distance d is consequently chosen to be 2736 nm (Fig. 4(a)), based on the results in Fig. 3. Congruent with those results, which are based on analysing the electric field at a single test point, Figs. 4(b)–4(e) show that the field enhancement is more pronounced at 1274 nm compared to 1224 nm across the whole gap between the two nanorails. The potential energy in Fig. 4(f) shows that the trapping depth at 1274 nm is more than twice of that at 1224 nm. As compared to the results on nanorails without any side grating (Fig. 2(d)), the trapping depth decreases by ~35% to 4.25 $k_B \cdot T/(mW \cdot \mu m^{-2})$ at 1224 nm and increases by ~22% to 9.35 $k_B \cdot T/(mW \cdot \mu m^{-2})$ at 1274 nm, a result of the destructive and constructive interference discussed in Fig. 3. Because the grating is present only on one side of the nanorails, the stable trapping positions of $F_x = 0$ deviate from the central points by ~ 60 nm (Fig. 4(g)).

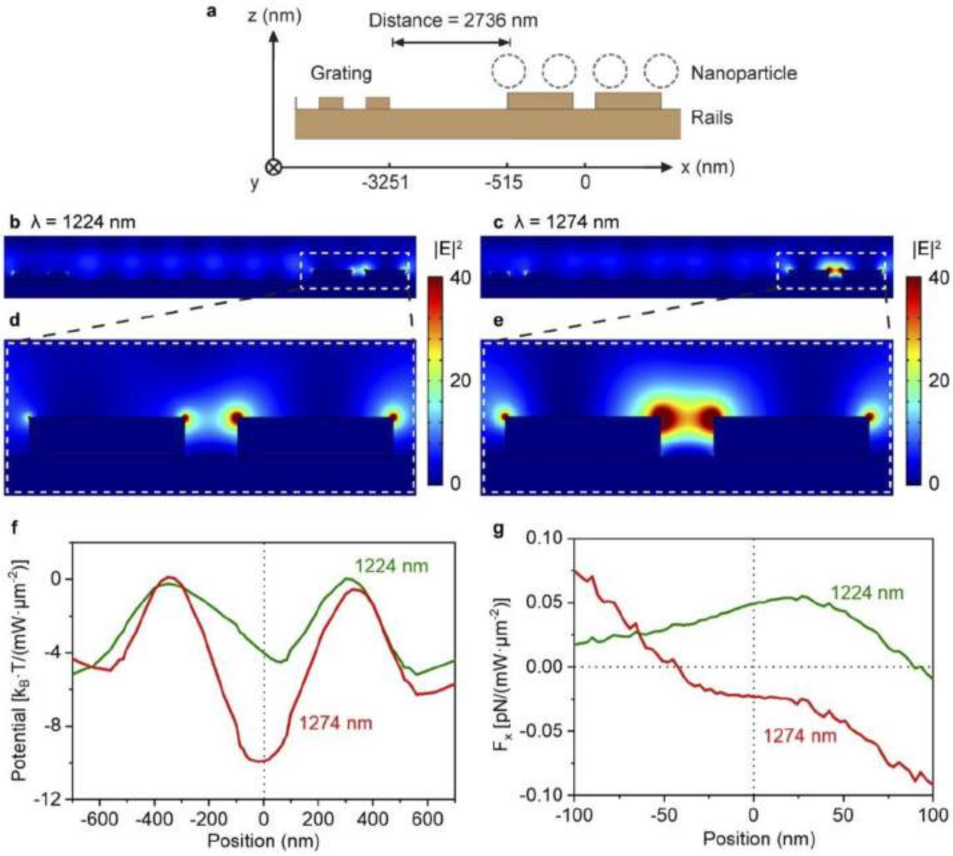

Fig. 4. Schematic diagram and trapping characteristics of Route 1. (a) Schematic of the nanostructure. The rail-grating distance d is 2736 nm. (b) Enhancement factor of the electric field density at 1224 nm as normalised against the incident field. The upper limit of colour scale is set to 40 for visualisation. The incident light is polarised along the x axis. (c) Corresponding distributions at 1274 nm. (d) A zoom-in view of panel b. (e) A zoom-in view of panel c. (f) Dependence of trapping potential energy on the central position of the nanoparticle. (g) Corresponding force F_x.

The bias of nanoparticle trapping between these two wavelengths can be reversed by selecting a different rail-grating distance d. Figure 5 shows the results for Route 2, which has $d = 2468$ nm.

As seen in Fig. 3, this value of d enables constructive and destructive interference at the centre of the two nanorails for 1224 nm and 1274 nm, respectively. The constructive interference at 1224 nm induces pronounced local field enhancement between the two rails (Figs. 5(b) and 5(d)) and a deep potential well of 10.57 k_B·T/(mW·μm^{-2}) (Fig. 5(f)). By comparison, the area with high field enhancement shrinks significantly at 1274 nm (Figs. 5(c) and 5(e)), and the well depth is only 5.55 k_B·T/(mW·μm^{-2}), about half of the depth at 1224 nm. Similar to Route 1, the stable points of $F_x = 0$ deviate from the centre of the two rails due to the break of mirror symmetry (Fig. 5(g)).

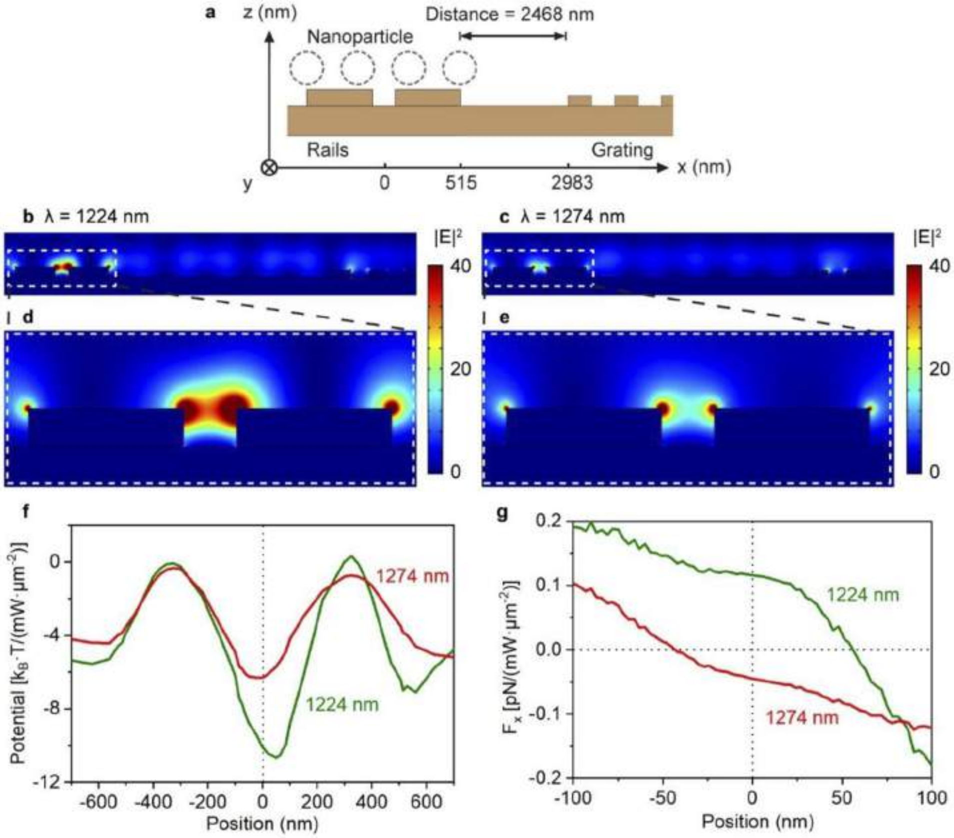

Fig. 5. Schematic and trapping characteristics of Route 2. The route has a rail-grating distance d of 2468 nm. The panels are plotted following the same specifications as Fig. 4.

5. Nanoparticle routing at the Y-branch junction

The wavelength sensitivity in the optical force shown in Figs. 4 and 5 is simulated for infinitely long nanorails, which approximate locations on the router not close to the Y-junction. Similar wavelength sensitivity is required at the junction, in order to guide the nanoparticle to the correct route (i.e. to Route 1 at 1274 nm and Route 2 at 1224 nm). This functionality is achieved by flanking the junction with the side gratings as shown in Fig. 1. If taking the tip of the Y-junction as $(x, y) = (0, 0)$, the two side gratings start at the line of $y \approx -1.5$ μm, which overlaps with the bottom edge of Figs. 6(a) and 6(c) (see Fig. 7 of the Appendix for exact dimensions). The polarisation of the incident light is changed from linear polarisation for the straight nanostrips to circular polarisation, owing to the planar curvature of the nanorails and gratings at the junction.

Figure 6(a) shows the distribution of electric field density at the *xy* plane 10 nm above the top of the rails. The wavelength of the incident light λ is 1274 nm. Similar to the results for straight nanorails shown in Figs. 2, 4 and 5, strong localised surface plasmonic resonance is observed at the edges of the nanorails. The line of strong field enhancement roughly traces the curvature of the Y-junction. Meanwhile, a clear difference between the two arms of the Y-junction can also be observed. The left arm is overall brighter than the right arm, and strong contrast is observed around the tip where the Entrance Route ends and the divergence of the two Routes starts. This contrast between the two arms indicates that the left arm is more effective in trapping the nanoparticle at $\lambda = 1274$ nm (Fig. 6(a)). This behaviour is confirmed in the calculation of F_x (Fig. 6(b)). Travelling along the centre of the Entrance Route, the nanoparticle is constantly directed to the left arm (i.e. Route 1) by the plasmonic near field. By comparison, Figs. 6(c) and 6(d) show the reverse situation: at $\lambda = 1224$ nm, the right arm (i.e. Route 2) of the Y-junction has stronger near-field enhancement than the left arm, and a nanoparticle at the same locations experiences optical force that directs it to the right arm. To further explore the functional range of the router, the refractive index of the nanoparticle is adjusted by 1.0, spanning from 1.4 to 2.4.

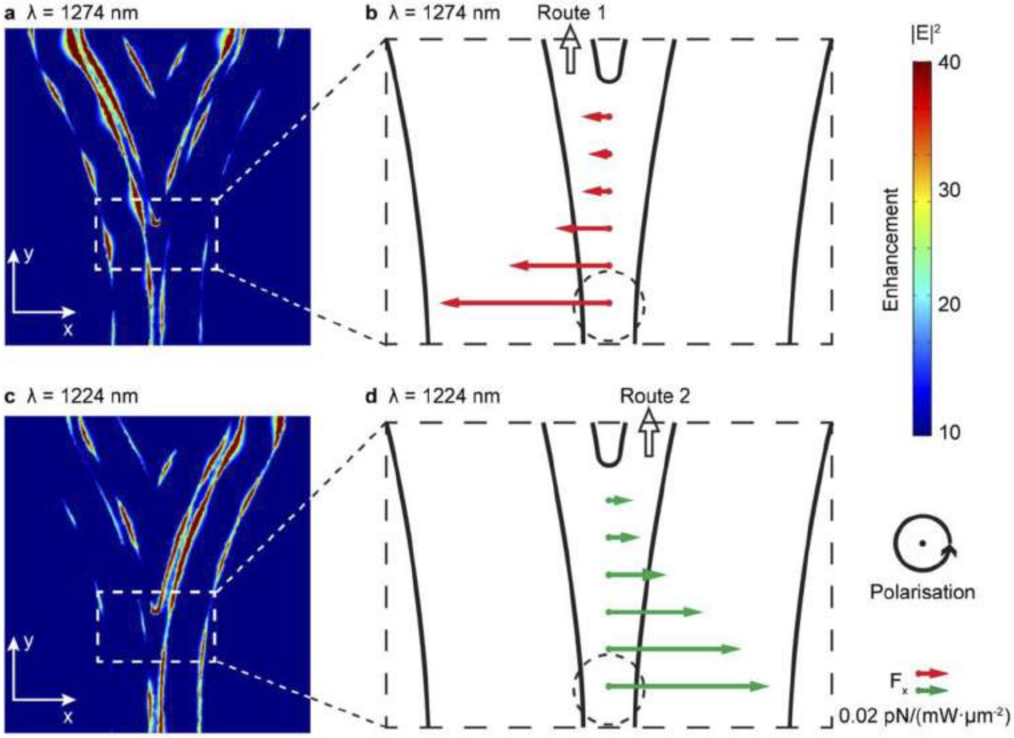

Fig. 6. Routing of the nanoparticle at the Y-branch junction. (a) The electric field density distribution at the *xy* plane 10 nm above the top surface of the nanorails. The electric field is normalised against the field of incident light. The upper and lower limits of colour scale are set at 40 and 10, respectively, for visualisation. The incident light is circularly polarised and the wavelength $\lambda = 1274$ nm. The start line of the two side gratings overlaps with the bottom edge of the figure. (b) Optical force along the *x* axis, F_x, with the nanoparticle (the black circle) at six evenly spaced, representative locations along the centre of the Y-branch junction. The scale is 0.02 pN/(mW·μm^{-2}). (c,d) Corresponding field distribution and force F_x at 1224 nm. The largest force at the six simulated locations is 0.11 pN/(mW·μm^{-2}) at both wavelengths.

The functionality of wavelength-dependent nanoparticle routing persists in the whole simulated range (see Fig. 8 of the Appendix for details).

The change to circular polarisation was made in order to highlight the influence of surface plasmons on nanoparticle trapping. In fact, neither the localised nor the propagating surface plasmons for the straight nanostrips can be excited by y-polarised incident light at these wavelengths. Consequently, if the incident light is changed to circulation polarisation for Figs. 2–5, the trapping potential and force, which have the normalised units of $\mathrm{k_B{\cdot}T/(mW{\cdot}\mu m^{-2})}$ and $\mathrm{pN/(mW{\cdot}\mu m^{-2})}$, respectively, decrease by 50%. As stable trapping requires a minimal potential depth (the guideline value ranges [42,43] from 1 $\mathrm{k_B{\cdot}T}$ to 10 $\mathrm{k_B{\cdot}T}$, which depends on the timescale of the trapping), this implies that circularly polarised light is less power efficient for the straight nanorails. Nevertheless, there is no change to the relative magnitude between the trapping efficiency at the two wavelengths of interest, and the whole nanoparticle route functions under the illumination of circularly polarised light.

6. Conclusion

In conclusion, a plasmonic nanoparticle router/switch actuated by the wavelength of incident light has been designed and demonstrated by numerical simulation. The router consists of a series of gold nanostrips on a plain gold thin film. It enables trapping, guiding and routing of nanoparticles in a continuous-flow microfluidic channel under the illumination of unfocused light at normal incidence. A nanoparticle can be guided to either one of two predefined routes, with a small change of 50 nm in the wavelength of the incident light. These functionalities are achieved by utilising the interference between localised and propagating surface plasmons induced on the gold nanostrips.

The design is simple, and has the potential to enable a cascaded, multi-route nanoparticle transport network that can be integrated with lab-on-a-chip devices. It can function at different wavelengths in a broad wavelength range, simply by scaling the dimensions of the plasmonic nanostructures. A key feature of the nanoparticle router is the combined use of plasmonic force and continuous liquid flow to achieve controlled nanoparticle transport. This scheme could improve nanoparticle manipulation efficiency as compared to pure plasmonic manipulation. It also addresses emerging requirements in advanced plasmonic nanoparticle manipulation that shift from controlling the position to controlling the motion of a nanoparticle. With the capability to trap and to transport, this new control scheme brings new opportunities in plasmonic nanoparticle manipulation, which may prove useful in various on-chip optofluidic applications.

Appendix

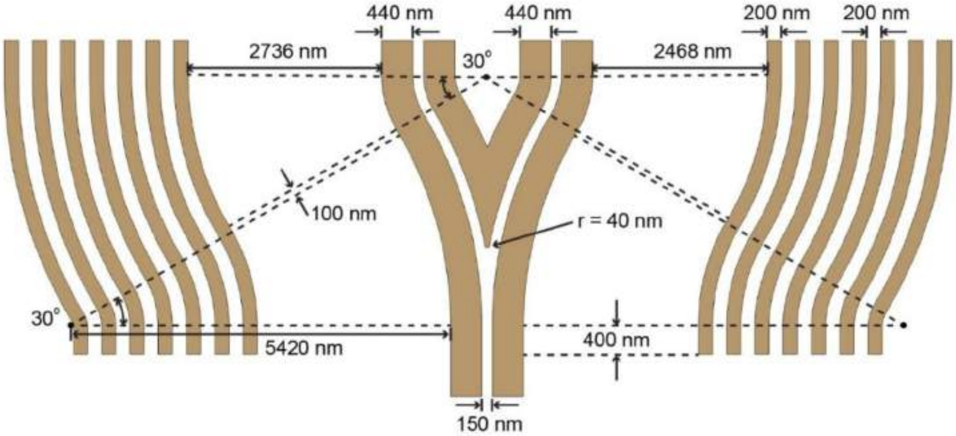

Fig. 7. Planar dimensions of the gold nanostrips at the Y-branch junction. The gold strips are on top of a plain gold thin film and consist of both curved and straight segments. The whole set of nanorails, including the Entrance Route, Route 1 and Route 2, possess mirror symmetry with respect to its central axis. The tip of the Y-junction has a radius of 40 nm. The two side gratings have a route-dependent rail-grating distance, which is 2736 nm for Route 1 and 2468 nm for Route 2.

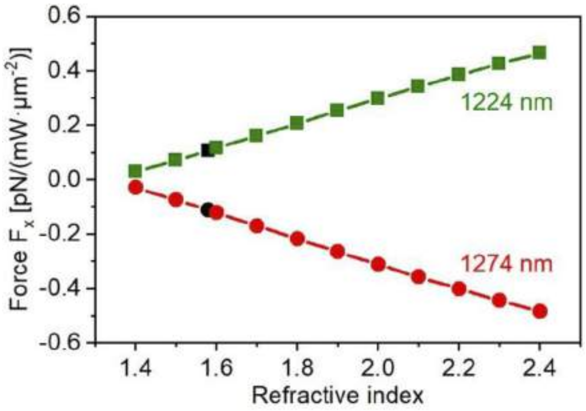

Fig. 8. Dependence of the optical force F_x on the refractive index of the nanoparticle. The nanoparticle is at the lowest of the six positions simulated in Fig. 6. The sign of the force indicates the direction, and a positive force directs the nanoparticle along the $+x$ direction (i.e. to Route 2). The two black symbols correspond to a refractive index of 1.58, the value discussed in the main text. At both wavelengths, the force scales linearly with the refractive index contrast between the nanoparticle and the liquid, and the sensitivity is ~0.45 pN/(mW·μm^{-2}) per unit change of the refractive index.

Funding

Royal Society (IEC\R3\183071, IES\R3\183086).

Data availability

The data that support the findings of this study are available from the corresponding author upon reasonable request.

Disclosures

The authors declare no conflicts of interest.

References

1. D. Gao, W. Ding, M. Nieto-Vesperinas, X. Ding, M. Rahman, T. Zhang, C. Lim, and C. W. Qiu, "Optical manipulation from the microscale to the nanoscale: fundamentals, advances and prospects," Light: Sci. Appl. **6**(9), e17039 (2017).
2. J. E. Baker, R. P. Badman, and M. D. Wang, "Nanophotonic trapping: precise manipulation and measurement of biomolecular arrays," WIREs Nanomed. Nanobiotechnol. **10**(1), e1477 (2018).
3. D. Erickson, X. Serey, Y. F. Chen, and S. Mandal, "Nanomanipulation using near field photonics," Lab Chip **11**(6), 995–1009 (2011).
4. O. M. Marago, P. H. Jones, P. G. Gucciardi, G. Volpe, and A. C. Ferrari, "Optical trapping and manipulation of nanostructures," Nat. Nanotechnol. **8**(11), 807–819 (2013).
5. X. Yang, Y. Liu, R. F. Oulton, X. Yin, and X. Zhang, "Optical forces in hybrid plasmonic waveguides," Nano Lett. **11**(2), 321–328 (2011).
6. O. G. Helleso, P. Lovhaugen, A. Z. Subramanian, J. S. Wilkinson, and B. S. Ahluwalia, "Surface transport and stable trapping of particles and cells by an optical waveguide loop," Lab Chip **12**(18), 3436–3440 (2012).
7. M. Soltani, J. Lin, R. A. Forties, J. T. Inman, S. N. Saraf, R. M. Fulbright, M. Lipson, and M. D. Wang, "Nanophotonic trapping for precise manipulation of biomolecular arrays," Nat. Nanotechnol. **9**(6), 448–452 (2014).
8. S. Lin, E. Schonbrun, and K. Crozier, "Optical manipulation with planar silicon microring resonators," Nano Lett. **10**(7), 2408–2411 (2010).
9. Y. Li, O. V. Svitelskiy, A. V. Maslov, D. Carnegie, E. Rafailov, and V. N. Astratov, "Giant resonant light forces in microspherical photonics," Light: Sci. Appl. **2**(4), e64 (2013).
10. N. Descharmes, U. P. Dharanipathy, Z. Diao, M. Tonin, and R. Houdre, "Single particle detection, manipulation and analysis with resonant optical trapping in photonic crystals," Lab Chip **13**(16), 3268–3274 (2013).
11. T. van Leest and J. Caro, "Cavity-enhanced optical trapping of bacteria using a silicon photonic crystal," Lab Chip **13**(22), 4358–4365 (2013).
12. S. H. Wu, N. Huang, E. Jaquay, and M. L. Povinelli, "Near-Field, On-Chip Optical Brownian Ratchets," Nano Lett. **16**(8), 5261–5266 (2016).
13. Z. Xu, W. Song, and K. B. Crozier, "Optical Trapping of Nanoparticles Using All-Silicon Nanoantennas," ACS Photonics **5**(12), 4993–5001 (2018).
14. J. Kim, "Joining plasmonics with microfluidics: from convenience to inevitability," Lab Chip **12**(19), 3611–3623 (2012).
15. A. Cuche, A. Canaguier-Durand, E. Devaux, J. A. Hutchison, C. Genet, and T. W. Ebbesen, "Sorting nanoparticles with intertwined plasmonic and thermo-hydrodynamical forces," Nano Lett. **13**(9), 4230–4235 (2013).
16. M. Wang, C. Zhao, X. Miao, Y. Zhao, J. Rufo, Y. J. Liu, T. J. Huang, and Y. Zheng, "Plasmofluidics: Merging Light and Fluids at the Micro-/Nanoscale," Small **11**(35), 4423–4444 (2015).
17. J. J. Baumberg, J. Aizpurua, M. H. Mikkelsen, and D. R. Smith, "Extreme nanophotonics from ultrathin metallic gaps," Nat. Mater. **18**(7), 668–678 (2019).
18. P. Genevet, J. Lin, M. A. Kats, and F. Capasso, "Holographic detection of the orbital angular momentum of light with plasmonic photodiodes," Nat. Commun. **3**(1), 1278 (2012).
19. X. Fang, M. L. Tseng, D. P. Tsai, and N. I. Zheludev, "Coherent Excitation-Selective Spectroscopy of Multipole Resonances," Phys. Rev. Appl. **5**(1), 014010 (2016).
20. X. Fang, K. F. MacDonald, E. Plum, and N. I. Zheludev, "Coherent control of light-matter interactions in polarization standing waves," Sci. Rep. **6**(1), 31141 (2016).
21. J. H. Kang, K. Kim, H. S. Ee, Y. H. Lee, T. Y. Yoon, M. K. Seo, and H. G. Park, "Low-power nano-optical vortex trapping via plasmonic diabolo nanoantennas," Nat. Commun. **2**(1), 582 (2011).
22. B. J. Roxworthy, K. D. Ko, A. Kumar, K. H. Fung, E. K. Chow, G. L. Liu, N. X. Fang, and K. C. Toussaint Jr., "Application of plasmonic bowtie nanoantenna arrays for optical trapping, stacking, and sorting," Nano Lett. **12**(2), 796–801 (2012).
23. K. Y. Chen, A. T. Lee, C. C. Hung, J. S. Huang, and Y. T. Yang, "Transport and trapping in two-dimensional nanoscale plasmonic optical lattice," Nano Lett. **13**(9), 4118–4122 (2013).
24. P. T. Lin, H. Y. Chu, T. W. Lu, and P. T. Lee, "Trapping particles using waveguide-coupled gold bowtie plasmonic tweezers," Lab Chip **14**(24), 4647–4652 (2014).
25. R. A. Jensen, I. C. Huang, O. Chen, J. T. Choy, T. S. Bischof, M. Lončar, and M. G. Bawendi, "Optical Trapping and Two-Photon Excitation of Colloidal Quantum Dots Using Bowtie Apertures," ACS Photonics **3**(3), 423–427 (2016).

26. Y. Zhao, A. A. E. Saleh, and J. A. Dionne, "Enantioselective Optical Trapping of Chiral Nanoparticles with Plasmonic Tweezers," ACS Photonics **3**(3), 304–309 (2016).
27. D. Yoo, K. L. Gurunatha, H. K. Choi, D. A. Mohr, C. T. Ertsgaard, R. Gordon, and S. H. Oh, "Low-Power Optical Trapping of Nanoparticles and Proteins with Resonant Coaxial Nanoaperture Using 10 nm Gap," Nano Lett. **18**(6), 3637–3642 (2018).
28. K. Wang, E. Schonbrun, P. Steinvurzel, and K. B. Crozier, "Scannable plasmonic trapping using a gold stripe," Nano Lett. **10**(9), 3506–3511 (2010).
29. P. Hansen, Y. Zheng, J. Ryan, and L. Hesselink, "Nano-optical conveyor belt, part I: Theory," Nano Lett. **14**(6), 2965–2970 (2014).
30. Y. Zheng, J. Ryan, P. Hansen, Y. T. Cheng, T. J. Lu, and L. Hesselink, "Nano-optical conveyor belt, part II: Demonstration of handoff between near-field optical traps," Nano Lett. **14**(6), 2971–2976 (2014).
31. Z. Kang, H. Lu, J. Chen, K. Chen, F. Xu, and H. P. Ho, "Plasmonic graded nano-disks as nano-optical conveyor belt," Opt. Express **22**(16), 19567–19572 (2014).
32. K. D. Leake, M. A. Olson, D. Ozcelik, A. R. Hawkins, and H. Schmidt, "Spectrally reconfigurable integrated multi-spot particle trap," Opt. Lett. **40**(23), 5435–5438 (2015).
33. P. R. Huft, J. D. Kolbow, J. T. Thweatt, and N. C. Lindquist, "Holographic Plasmonic Nanotweezers for Dynamic Trapping and Manipulation," Nano Lett. **17**(12), 7920–7925 (2017).
34. M. Jiang, G. Wang, W. Jiao, Z. Ying, N. Zou, H. P. Ho, T. Sun, and X. Zhang, "Plasmonic non-concentric nanorings array as an unidirectional nano-optical conveyor belt actuated by polarization rotation," Opt. Lett. **42**(2), 259–262 (2017).
35. M. Jiang, G. Wang, W. Xu, W. Ji, N. Zou, H. P. Ho, and X. Zhang, "Two-dimensional arbitrary nano-manipulation on a plasmonic metasurface," Opt. Lett. **43**(7), 1602–1605 (2018).
36. J. C. Ndukaife, A. V. Kildishev, A. G. Nnanna, V. M. Shalaev, S. T. Wereley, and A. Boltasseva, "Long-range and rapid transport of individual nano-objects by a hybrid electrothermoplasmonic nanotweezer," Nat. Nanotechnol. **11**(1), 53–59 (2016).
37. L. Lin, M. Wang, X. Peng, E. N. Lissek, Z. Mao, L. Scarabelli, E. Adkins, S. Coskun, H. E. Unalan, B. A. Korgel, L. M. Liz-Marzan, E. L. Florin, and Y. Zheng, "Opto-thermoelectric nanotweezers," Nat. Photonics **12**(4), 195–201 (2018).
38. E. Hendry, P. J. Hale, J. Moger, A. K. Savchenko, and S. A. Mikhailov, "Coherent nonlinear optical response of graphene," Phys. Rev. Lett. **105**(9), 097401 (2010).
39. P. B. Johnson and R. W. Christy, "Optical Constants of the Noble Metals," Phys. Rev. B **6**(12), 4370–4379 (1972).
40. K. Wang, E. Schonbrun, P. Steinvurzel, and K. B. Crozier, "Trapping and rotating nanoparticles using a plasmonic nano-tweezer with an integrated heat sink," Nat. Commun. **2**(1), 469 (2011).
41. X. Li, Q. Tan, B. Bai, and G. Jin, "Non-spectroscopic refractometric nanosensor based on a tilted slit groove plasmonic interferometer," Opt. Express **19**(21), 20691–20703 (2011).
42. M. L. Juan, R. Gordon, Y. Pang, F. Eftekhari, and R. Quidant, "Self-induced back-action optical trapping of dielectric nanoparticles," Nat. Phys. **5**(12), 915–919 (2009).
43. M. L. Juan, M. Righini, and R. Quidant, "Plasmon nano-optical tweezers," Nat. Photonics **5**(6), 349–356 (2011).